The Astrophysical Journal, 788:66 (15pp), 2014 June 10 doi:10.1088/0004-637X/788/1/66

THE OH ROTATIONAL POPULATION AND PHOTODISSOCIATION OF H_2O IN DG Tauri

John S. Carr[1] and Joan R. Najita[2,3]
[1] Naval Research Laboratory, Code 7211, Washington, DC 20375, USA
[2] National Optical Astronomy Observatory, 950 North Cherry Avenue, Tucson, AZ 85716, USA
[3] Institute for Theory and Computation, Harvard-Smithsonian Center for Astrophysics, 60 Garden Street, Cambridge, MA 02138, USA
Received 2013 December 11; accepted 2014 April 23; published 2014 May 22

ABSTRACT

We analyze the OH rotational emission in the *Spitzer Space Telescope* mid-infrared spectrum of the T Tauri star DG Tau. OH is observed in emission from upper level energies of 1900 K to 28,000 K. The rotational diagram cannot be fit with any single combination of temperature and column density and has slopes that correspond to excitation temperatures ranging from 200 K to 6000 K. The relative Λ-doublet population within each rotational level is not equal, showing that the OH population is not in thermal equilibrium. The symmetric Λ-doublet state is preferred in all rotational states, with an average of 0.5 for the population ratio of the anti-symmetric to symmetric state. We show that the population distribution of the high rotational lines and the Λ-doublet ratio are consistent with the formation of OH following the photo-dissociation of H_2O by FUV photons in the second absorption band of water (∼1150–1400 Å), which includes Lyα. Other processes, OH formation from either photo-dissociation of water in the first absorption band (1450–1900 Å) or the reaction O(^1D) + H_2, or collisional excitation, cannot explain the observed emission in the high rotational states but could potentially contribute to the population of lower rotational levels. These results demonstrate that the photodissociation of water is active in DG Tau and support the idea that the hot rotational OH emission commonly observed in Classical T Tauri stars is due to the dissociation of H_2O by FUV radiation.

Key words: accretion, accretion disks – infrared: stars – circumstellar matter – protoplanetary disks – stars: pre-main sequence

Online-only material: color figures

1. INTRODUCTION

An important development in the study of the molecular gas within protoplanetary disks was the finding that emission from warm water is very common in the mid-infrared spectra of classical T Tauri stars (Carr & Najita 2008; Salyk et al. 2008; Pontoppidan et al. 2010b; Carr & Najita 2011, hereafter CN11). The LTE analyses of spectra obtained with the *Spitzer Space Telescope* find temperatures ∼ 500 K, water column densities ∼ 10^{18} cm^{-2}, and projected emitting areas with radii ∼ 1 AU (Carr & Najita 2008; CN11; Salyk et al. 2011). These parameters, along with limited kinematic data (Pontoppidan et al. 2010a; Knez et al. 2007), are consistent with the water emission originating in a warm molecular disk atmosphere inside of the snowline. Hence, water vapor is both common and abundant in the inner disk region, at least in the upper disk atmosphere.

The H_2O emission spectrum in classical T Tauri stars (CTTS) is accompanied by emission in the rotational lines of OH. For the longer wavelength lines accessible with *Spitzer*, the OH emission is characterized by rotational temperatures of 500–1200 K (Carr & Najita 2008; Salyk et al. 2011; Banzatti et al. 2012). In contrast, the higher rotational lines at shorter wavelengths indicate rotational temperatures of a few thousand K (Najita et al. 2010; CN11; Banzatti et al. 2012), a factor of 10 higher than the temperatures derived for H_2O and other molecules measured in the *Spitzer* spectra. Najita et al. (2010; CN11) proposed that these highly excited rotational levels are populated following the formation of OH by FUV photodissociation of H_2O. A correlation between the flux of the highly excited OH emission and the mass accretion rate (CN11), which is derived from the UV excess in CTTS, further supports a role for FUV in producing the OH emission.

Bethell & Bergin (2009) pointed out that the derived column densities of water are high enough to shield lower levels of the disk atmosphere from the photodissociating effects of FUV radiation, even in a dust-depleted atmosphere. In their simple self-shielding model, a layer of high OH column density is produced as a consequence of photodissociation of H_2O, and the maximum OH column density is limited by the FUV opacity due to OH and H_2O self-shielding. This self-shielding process could be fundamental to the survival of water closer to the disk midplane and to the sheltering of a potentially rich organic chemistry from FUV radiation. The absorption of FUV photons by water could also play an important role in the thermodynamics of the warm molecular layer (Bethell & Bergin 2009; Najita et al. 2011; Ádámkovics et al. 2014). Direct evidence for the photodissociation of water and the role of molecular shielding is therefore of great interest, and the rotational lines of OH provide a potential diagnostic of these processes.

Emission from OH has been used as a probe of H_2O photodissociation in other contexts. The OH molecule has long served as an important proxy for water in comets. While water is the dominant volatile species from active cometary nuclei, it has historically been difficult to observe. Because OH is a direct photodissociation product of water, it has been used extensively to determine the production rate of water in comets, mainly from photometric and spectroscopic measurements of the UV bands and radio observations of the 18 cm lines (A'Hearn et al. 1995; Crovisier 1989; Crovisier et al. 2002; Combi et al. 2004; Feldman et al. 2004). Of more direct relevance to this paper are recent observations of infrared OH prompt emission, in particular the detailed studies of Bonev and collaborators (Bonev et al. 2006; Bonev & Mumma 2006) based on near-infrared echelle spectra of the 3 μm rovibrational transitions.

Highly excited OH rotational emission has also been detected in *Spitzer* spectra of the terminal shocks of protostellar jets, as first found in HH 211 and later reported in two other Herbig–Haro objects (Tappe et al. 2008, 2012). This emission is likely due to OH formed by the photodissociation of H_2O, with the FUV radiation generated in the shock. The H_2O could originate from either photodesorption of ice from grains or chemistry in the shocked gas.

The mid-infrared *Spitzer* spectrum of DG Tau provides a special opportunity to study in detail the rotational OH emission in protoplanetary disks. While H_2O dominates the *Spitzer* spectra of most CTTS, the water emission in DG Tau is very weak compared to the OH emission, possibly a consequence of the high accretion rate and large UV excess (CN11). This results in a relatively clean OH spectrum over the entire wavelength coverage of the *Spitzer* spectrum, enabling study of the rotational population over a wide range in energy level. We will show that information on the population distribution of the OH Λ-doublets can also be derived from these data, providing an additional diagnostic on the pathway by which the OH is produced.

DG Tau is an extremely active CTTS with a high accretion rate, a large optical and UV excess, and a well studied jet. In the near-infrared, DG Tau often shows CO overtone emission indicative of hot molecular gas, though this emission varies and is not always present (Carr 1989; Biscaya et al. 1997; Horne et al. 2012). Emission from hot H_2O has also been reported (Najita et al. 2000), similar to the ∼1500 K water emission observed in some other CO overtone emitting CTTS (Carr et al. 2004; Doppmann et al. 2011). Low-excitation H_2O lines have recently been detected in the far-infrared with the Herschel Space Observatory (Podio et al. 2012; 2013; Fedele et al. 2013); these lines may originate in cool gas in the outer disk.

2. SPITZER IRS SPECTROSCOPY

The mid-infrared spectra analyzed in this study were obtained with the *Spitzer* Infrared Spectrograph (IRS; Houck et al. 2004) as part of *Spitzer* GO program 2300. DG Tau was observed in staring mode in the short–high (SH; 10–19 μm) and long–high (LH; 19–37 μm) modules, which have a nominal resolving power of ∼600. The frame time was 6.3 s for both modules, with total integration times of 302 s on target and 151 s on sky. The data reduction procedure is described in detail in CN11. The combination of the redundancy provided by the large number of cycles and the optimized data processing procedures allow high S/N ratios to be attained. For DG Tau, the S/N ratios on the continuum range from 300 to 600 in the SH spectrum, and from 200 to 400 in the LH spectrum.

The SH spectrum was previously presented in CN11. DG Tau lacks the prominent H_2O emission commonly seen in classical T Tauri stars but does show rotational OH emission. OH emission lines are present throughout the entire wavelength span of the SH and LH modules, covering a wide range in rotational levels. While CN11 gave an upper limit on H_2O emission for DG Tau, we will show in Section 6 that weak water emission lines are present in its spectrum. The SH spectrum has exceptionally strong [Ne II] emission (which may originate from a jet; see Guedel et al. 2010; CN11), H I emission lines, and [Fe II] emission at 17.93 μm. Atomic lines that are present in the LH spectrum include [Fe II] at 24.5 and 26.0 μm, and [Si II] at 34.82 μm.

3. OH SPECTRAL MEASUREMENTS

Measurements of the OH emission were facilitated by the fitting and subtraction of a continuum within the vicinity of each OH feature. The continuum regions excluded the wavelength intervals with OH and other known or suspected emission features. The OH line fluxes were measured by summing over the pixels covering the wavelength extent of the OH feature, as determined by comparison to synthetic spectra calculated with the spectral resolution and sampling of the IRS. Two methods were used to estimate the noise in the spectrum. In the first, the average spectra from the two nod positions were differenced, and the pixel rms was measured to determine the noise in the final average spectrum as a function of wavelength. In the second, the rms was measured over the region used for the continuum fit for each OH feature. The average of these two estimates was used or, in cases where the latter method gave a higher noise, the larger value was adopted.

The continuum-subtracted spectra of the OH emission lines are shown in Figures 1 and 2, and the measured OH line fluxes are given in Table 1. The transitions are ordered by the upper state quantum number N, the total angular momentum apart from spin. The electronic ground state of OH is $^2\Pi$, and spin–orbit coupling splits the rotational states into two ladders, labeled $^2\Pi_{3/2}$ and $^2\Pi_{1/2}$, with the total angular momentum given by $J = N \pm 1/2$, respectively. There is an additional splitting of the rotational levels by Λ-doubling. Hence, the OH rotational transitions in the mid-infrared appear as quadruplets for each value of N. The wavelengths of these four individual components for each N are marked in Figure 1.

Emission from OH is detected over the entire wavelength range of the IRS high-resolution modules. These transitions cover a wide range in rotational excitation, from $E_{up} = 1900$ K at $N_{up} = 8$, to $E_{up} = 28{,}000$ K at $N_{up} = 34$. In addition to the main ladder rotational transitions, three cross-ladder transitions were detected in LH (Figure 2 and Table 1), with E_{up} from 600 K to 1190 K. Because the transition probabilities for these cross-ladder transitions are ∼50 times less than the transition probabilities for the main-ladder transitions from the same levels, the substantial line fluxes measured in the cross-ladder lines indicate that the low excitation main-ladder transitions are optically thick.

While a large range in excitation energy for the rotational OH lines in CTTS has previously been pointed out, the spectrum of DG Tau provides a clear view of the entire rotational ladder within the IRS bandpass. A similar *Spitzer* spectrum of rotationally excited OH is observed in the Herbig–Haro object HH 211, although in that case the highest energy lines appear to have a larger relative intensity (see Figure 2 in Tappe et al. 2012).

Some of the OH emission features may be blended with emission from other species. The H I line at 11.31 μm almost certainly contributes to the OH at $N = 28$, based on the strength of the 12.37 μm H I line and the H I line ratios seen in the T Tauri stars. Water emission lines fall within both the $N = 32$ and $N = 18$ OH features and could potentially account for the somewhat higher flux in these lines. There is also a strong red wing to the $N = 32$ OH emission feature and a fairly strong blue wing to the $N = 26$ feature.

The Λ-doublet components are labeled as to their symmetry with respect to reflection in the plane of rotation of the molecule (Alexander & Dagdigian 1984; Alexander et al. 1988). States that are symmetric with respect to reflection in the plane of rotation are referred to as $\Pi(A')$, while those that are

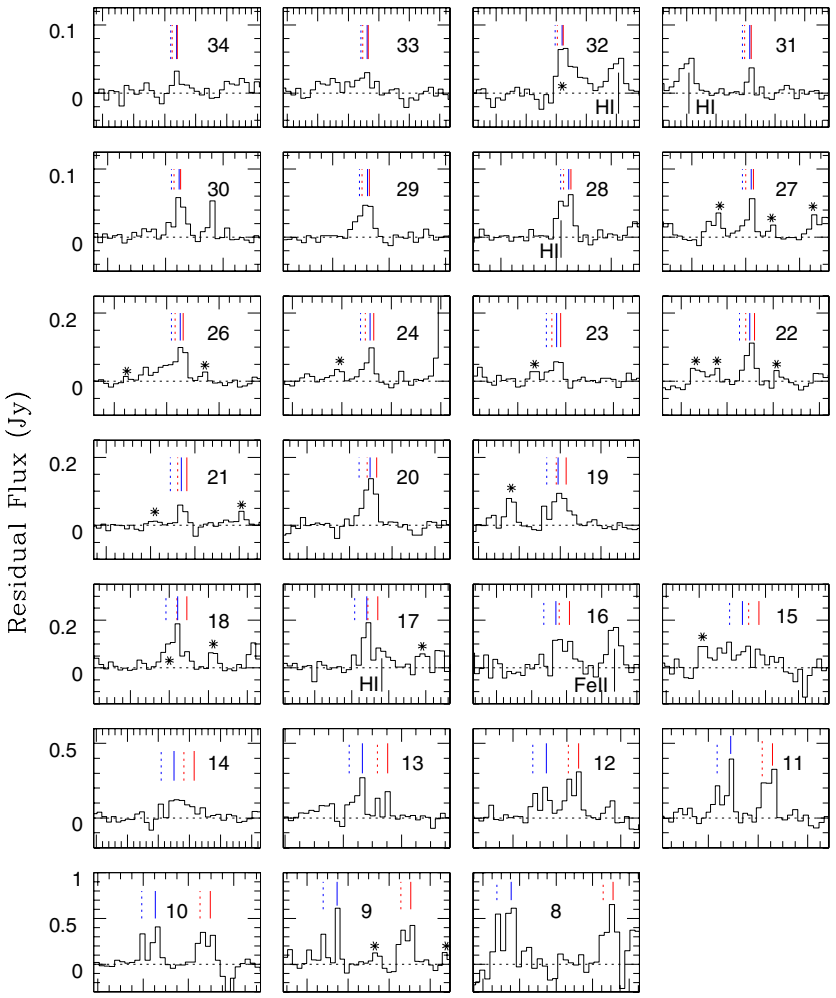

Figure 1. Continuum subtracted spectra of the rotational OH transitions observed in the *Spitzer* IRS spectrum of DG Tau. The transitions are labeled by the upper rotational number N (total angular momentum without spin), and each panel displays a 8000 km s^{-1} velocity extent centered on the average wavelength of the four spin-orbit and Λ-doublet components. Vertical blue lines mark the positions of the $^2\Pi_{3/2}$ ladder transitions, and red lines mark positions of the $^2\Pi_{1/2}$ ladder transitions. Dashed lines indicate transitions within the A'' Λ-doublet levels, states that are antisymmetric with respect to reflection in the plane of rotation of the molecule; solid lines indicate transitions in the symmetric A' Λ-doublet levels. Atomic transitions of H I and [Fe II] are labeled, and the locations of identified or suspected H_2O transitions are marked with a (∗).

(A color version of this figure is available in the online journal.)

antisymmetric with respect to reflection in the plane of rotation are $\Pi(A'')$. In the $^2\Pi_{3/2}$ ladder, the e doublet levels are symmetric (A'), while the f levels are antisymmetric (A'') (using the standard spectroscopic e/f labeling). This is reversed in the $^2\Pi_{1/2}$ ladder, where the f levels are symmetric (A') and the e doublet levels are antisymmetric (A''). The different spin–orbit and Λ-doublet components are identified in Figure 1.

For low values of N (longer wavelength transitions), the spin components in the IRS spectra are well separated in wavelength. The Λ-doublets have a greater wavelength separation in the $^2\Pi_{3/2}$ component, and from $N = 8$ to 12 the Λ-doublets in the $^2\Pi_{3/2}$ ladder are spectrally resolved. As N increases, the wavelength separation of the spin and Λ-doublet components gradually decreases and the components become fully blended in the IRS spectra.

A close study of the spectra in Figure 1 shows that the Λ-doublet levels are not equally populated. This is most clearly seen in the $^2\Pi_{3/2}$ components from $N = 8$ to 12. For each of these Λ-doublets, the antisymmetric A'' transition (f level) is weaker than the A' transition (e level). Even when the individual components are not spectrally resolved, an asymmetry in the intensity of the Λ-doublets can be discerned. At intermediate N (e.g., $N = 20$–22), the wavelength separation of the components is large enough that the OH blend should be broader than the spectral resolution. Instead, the observed emission features are narrower than expected for the case where the four components have equal intensity; in addition, the line centroid is shifted from the mean wavelength of the components in the direction of the A' transitions.

For those rotational levels where the $^2\Pi_{3/2}$ Λ-doublets are spectrally resolved, the measured flux ratios were used to calculate the population ratio of the A'' to A' levels, under the assumption that the emission is optically thin. The result in Figure 3(a) shows a clear preference for the symmetric A' level. The average ratio of the $\Pi(A'')$ to $\Pi(A')$ Λ-doublet states of 0.68. Figure 3(b) shows the spin population ratio for the same rotational levels. The result is consistent with equal population in the $^2\Pi_{3/2}$ and $^2\Pi_{1/2}$ states.

4. LAMBDA-DOUBLET RATIOS

The Λ-doublets are blended for the majority of rotational levels N. In order to determine the relative Λ-doublet populations over the full range of rotational levels covered by the IRS spectra,

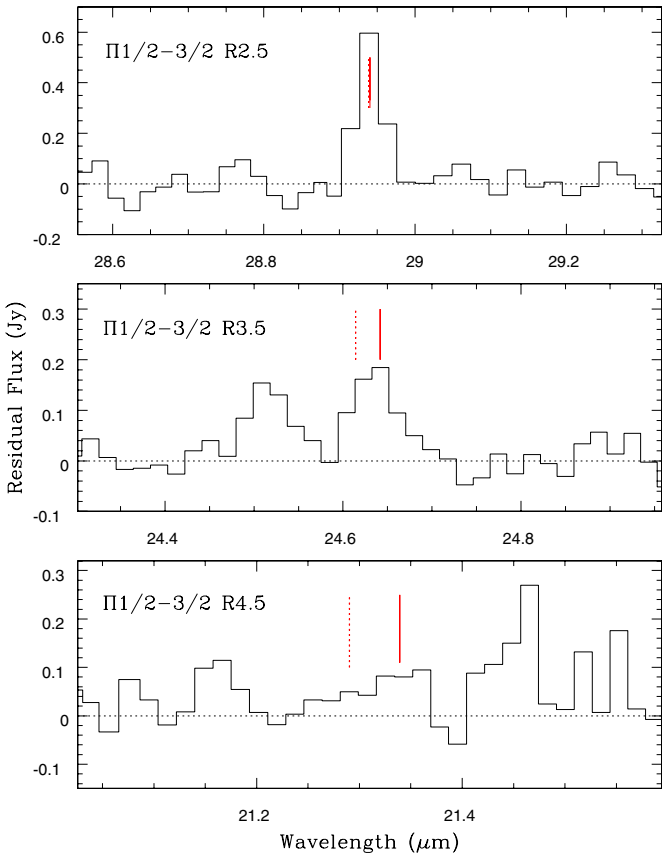

Figure 2. Continuum subtracted spectra of the cross-ladder rotational transitions of OH observed in the *Spitzer* LH spectrum of DG Tau. The upper states for these transitions are in the $^2\Pi_{1/2}$ ladder. Dashed lines indicate transitions within the antisymmetric A'' Λ-doublet levels, and solid lines indicate transitions in the symmetric A' Λ-doublet levels.

(A color version of this figure is available in the online journal.)

synthetic spectra were calculated and fit to the observed OH features. The procedures for calculating the synthetic spectra are similar to those described in CN11, except that the OH column density is specified separately for the Π(A'') and Π(A') Λ-doublet states. The transition data for OH are from the HITRAN database (Rothman et al. 2005). For each OH feature, spectra were calculated for a range in the A'' to A' population ratio, while keeping the total flux fixed to the measured value (Table 1). The best-fit value for the population ratio and its confidence intervals were determined by calculating χ^2 between the observed and model spectra. The derived A'' to A' ratios assume that the OH transitions are optically thin.

Examples of calculated spectra and best fits to the data are shown in Figure 4 for three values of N. These examples cover three cases: the Λ-doublets in the $^2\Pi_{3/2}$ ladder are spectrally resolved ($N = 11$); the four components are blended, but the OH blend is expected to be spectrally resolved ($N = 20$); the OH blend is expected to be unresolved ($N = 30$). The upper panels in Figure 4 show model spectra with equal Λ-doublet populations, while the lower panels show model spectra using the Λ-doublet ratios that gave minimum χ^2. The best-fit Λ-doublet ratios for all N are given in Table 2. Some lines were excluded from consideration: $N = 33$ and 34 due to low S/N, $N = 32$ due to likely blending, and $N = 28$ due to the blend with H I emission. The $N = 18$ line is included in Table 2, but it does has a potential blend with H_2O. For the six lowest values of N, Λ-doublet ratios could be derived separately for the $^2\Pi_{3/2}$ and $^2\Pi_{1/2}$ ladders; for these, the A'' to A' ratios generally agree within the uncertainties. In addition, the A'' to A' ratios from the spectral fits are in agreement with those determined directly from the measured flux ratios for the five Λ-doublets of the $^2\Pi_{3/2}$ ladder shown in Figure 3(a). Among the three cross-ladder transitions, two lines in Figure 2 show a Λ-doublet asymmetry, while the components are coincident in wavelength for the third (R2.5) line. A value is only reported for the R3.5 line, since the results were very uncertain for the R4.5 line.

The relative population in the Λ-doublet states is plotted as a function of N in Figure 5. A weighted average is plotted for the six values of N where separate ratios were derived for the two rotational ladders. The $N = 18$ line is an outlier with large errors, possibly due to a blend with H_2O, and is not plotted. The Λ-doublets in DG Tau show a consistent preference for the symmetric A' state of OH, with an average Π(A'') to Π(A') ratio of about 0.5. There appears to be a trend in the plot, with a larger

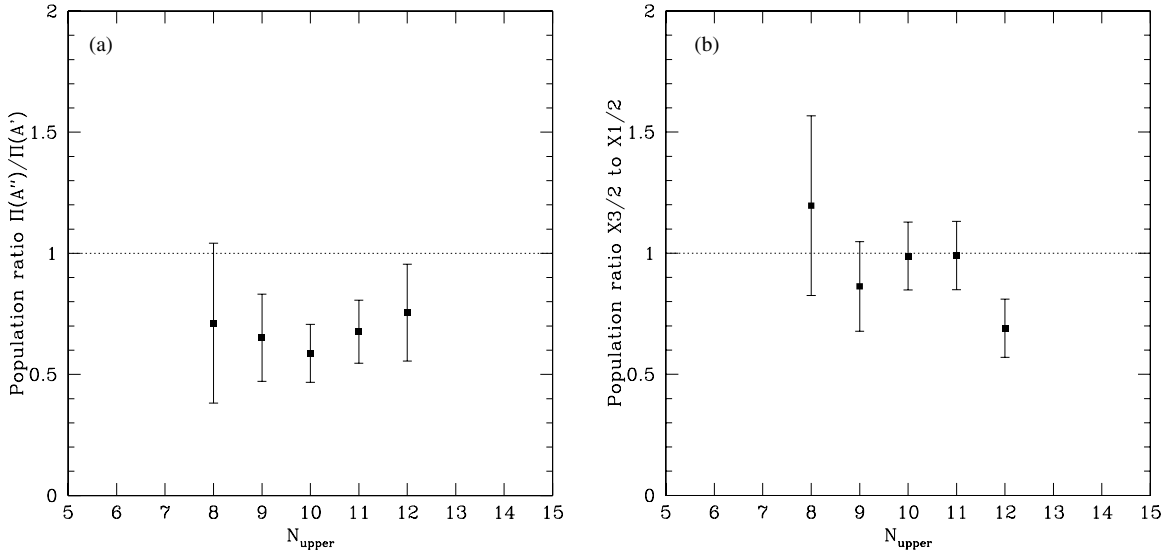

Figure 3. (a) The Λ-doublet population ratio of the A'' to A' levels, based on individually measured fluxes of the Λ-doublet components in the $^2\Pi_{3/2}$ state which are spectrally resolved. The average ratio of the Π(A'') to Π(A') states is 0.68. (b) The population ratio of the spin states, $^2\Pi_{3/2}$ to $^2\Pi_{1/2}$, for the same values of N. The average ratio is consistent with unity.

Table 1
Measured OH Transitions and Fluxes

λ (μm)	N_{up}	Flux (10^{-17} W m^{-2})	E_{up} (K)	OH Transitions
10.07	34	1.33 ± 0.48	28182	3/2 R33.5ef, 1/2 R32.5ef
10.23	33	1.80 ± 0.46	26752	3/2 R32.5ef, 1/2 R31.5ef
10.40	32	3.09 ± 0.40[a]	25344	3/2 R31.5ef, 1/2 R30.5ef
10.60	31	1.15 ± 0.32	23961	3/2 R30.5ef, 1/2 R29.5ef
10.82	30	3.02 ± 0.31	22608	3/2 R29.5ef, 1/2 R28.5ef
11.06	29	3.49 ± 0.35[b]	21274	3/2 R28.5ef, 1/2 R27.5ef
11.30	28	4.29 ± 0.35[c]	19976	3/2 R27.5ef, 1/2 R26.5ef
11.60	27	2.15 ± 0.46	18702	3/2 R26.5ef, 1/2 R25.5ef
11.92	26	5.76 ± 0.44[b]	17463	3/2 R25.5ef, 1/2 R24.5ef
12.65	24	4.10 ± 0.42	15084	3/2 R23.5ef, 1/2 R22.5ef
13.08	23	3.12 ± 0.39	13944	3/2 R22.5ef, 1/2 R21.5ef
13.54	22	4.51 ± 0.54	12844	3/2 R21.5ef, 1/2 R20.5ef
14.06	21	2.12 ± 0.57	11784	3/2 R20.5ef, 1/2 R19.5ef
14.64	20	6.70 ± 0.66	10760	3/2 R19.5ef, 1/2 R18.5ef
15.29	19	5.77 ± 0.58	9775	3/2 R18.5ef, 1/2 R17.5ef
16.02	18	8.20 ± 0.63[a]	8836	3/2 R17.5ef, 1/2 R16.5ef
16.84	17	6.92 ± 0.69	7943	3/2 R16.5ef, 1/2 R15.5ef
17.77	16	6.10 ± 0.98	7082	3/2 R15.5ef, 1/2 R14.5ef
18.84	15	5.85 ± 1.23	6273	3/2 R14.5ef, 1/2 R13.5ef
20.06	14	7.82 ± 1.56	5513	3/2 R13.5ef, 1/2 R12.5ef
21.44	13	7.30 ± 1.04	4773	3/2 R12.5ef
21.53	13	3.85 ± 1.03	4817	1/2 R11.5ef
23.07	12	2.65 ± 0.56	4105	3/2 R11.5f
23.12	12	3.48 ± 0.56	4092	3/2 R11.5e
23.22	12	8.84 ± 1.06	4147	1/2 R10.5ef
25.04	11	3.54 ± 0.57	3476	3/2 R10.5f
25.09	11	5.19 ± 0.57	3475	3/2 R10.5e
25.24	11	8.65 ± 0.89	3529	1/2 R9.5ef
27.39	10	3.79 ± 0.68	2904	3/2 R9.5f
27.45	10	6.40 ± 0.68	2903	3/2 R9.5e
27.67	10	10.10 ± 1.02	2957	1/2 R8.5ef
30.28	9	3.33 ± 0.78	2378	3/2 R8.5f
30.35	9	5.07 ± 0.78	2377	3/2 R8.5e
30.68	9	9.52 ± 1.24	2442	1/2 R7.5ef
33.88	8	6.24 ± 2.32	1910	3/2 R7.5f
33.95	8	8.68 ± 2.31	1898	3/2 R7.5e
34.48	8	12.07 ± 2.65	1972	1/2 R6.5ef
		Cross-Ladder Transitions		
21.31	6	4.39 ± 1.13	1186	1/2–3/2 R4.5ef
24.63	5	5.05 ± 0.64	874	1/2–3/2 R3.5ef
28.94	4	9.19 ± 0.72	613	1/2–3/2 R2.5ef

Notes.
[a] Coincident H_2O line potentially contributes to measured flux.
[b] Blue wing to OH feature.
[c] Emission from H I contributes to the measured flux.

ratio at low N than at high N. For $N \leqslant 20$, the $\Pi(A'')$ to $\Pi(A')$ ratio is 0.66 ± 0.12 (std), while for $N > 20$, the average ratio is 0.38 ± 0.20.

While this difference between high and low N could reflect an intrinsically higher A'' to A' ratio at low N, such an effect could be produced by higher optical depth in lower rotational lines. The Λ-doublet ratios were derived assuming the lines are optically thin. However, if the transitions become very optically thick, then the intensities of the Λ-doublet components will be driven toward unity, even with an intrinsic inversion in the Λ-doublet population. Therefore, the derived Λ-doublet ratio is an upper limit to the intrinsic ratio. For example, some test spectral modeling showed that modest optical depths, $\tau \sim 1$–3, would be sufficient to produce an apparent $\Pi(A'')/\Pi(A')$ ratio of 0.6 given an intrinsic ratio of 0.4.

5. ROTATION DIAGRAM

A standard rotation diagram is presented in Figure 6 for the OH emission in DG Tau. The rotation diagram clearly shows that a single temperature optically thin component cannot describe the rotational excitation of OH over the observed range in upper energy level. Some linear fits are shown in Figure 6 that illustrate the range of rotational temperatures that can describe the OH population. The fit to the population with $N > 20$ gives a rotational temperature of about 6300 K. This result is similar to the rotationally hot OH population commonly seen in the IRS spectra of CTTS (CN11), which was a basis for the suggestion that the OH is a photodissociation product of H_2O. The low rotational transitions ($N < 16$) fall close to a line, and a linear fit to these yields 1000 K for the rotational temperature. Similar

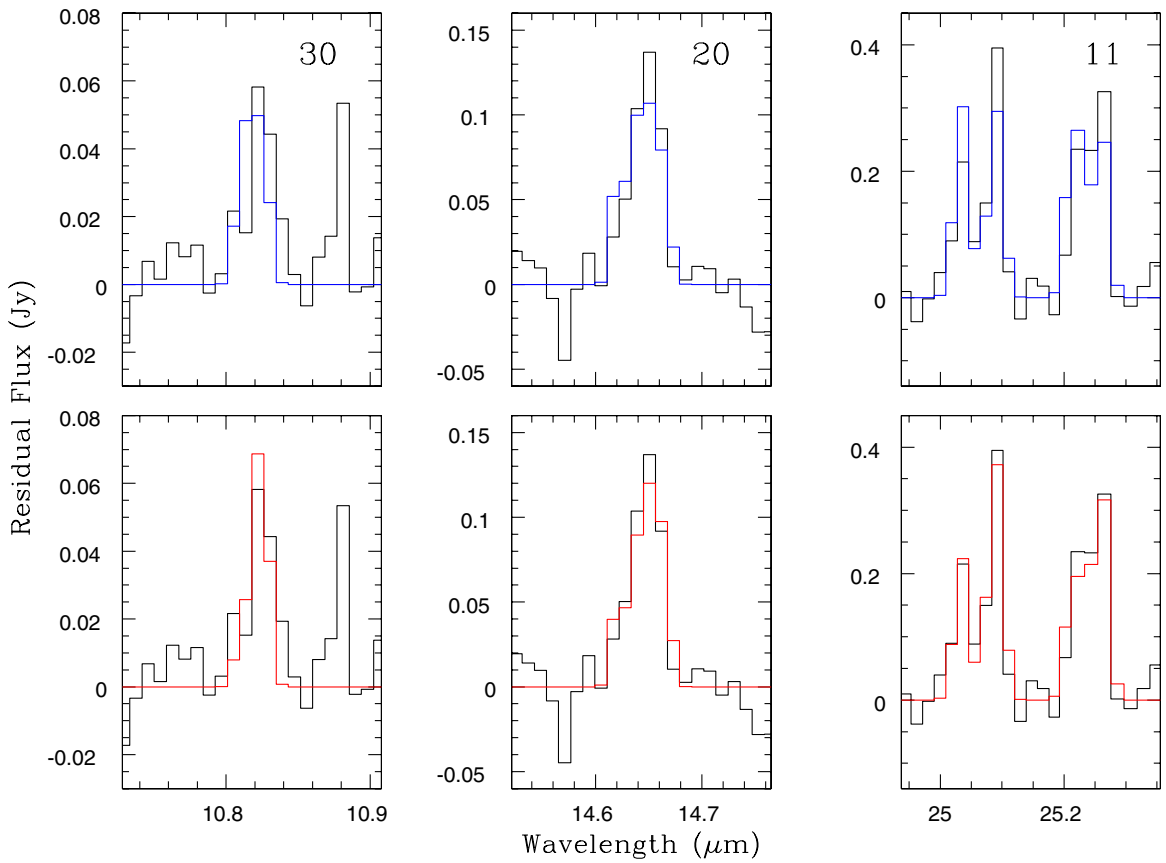

Figure 4. Examples of spectral fits used to derive Λ-doublet population ratios from the observed spectra. For each value of N plotted, the top row shows model spectra (blue histogram) with equal populations in the Λ-doublet levels compared to the continuum subtracted OH spectra (black histogram). The bottom row shows the model spectra (red histogram) with the Λ-doublet ratio ($\Pi(A'')/\Pi(A')$) that gave the best fit (minimum χ^2) to the observed spectrum. See Table 2 for a list of the Λ-doublet ratios.

(A color version of this figure is available in the online journal.)

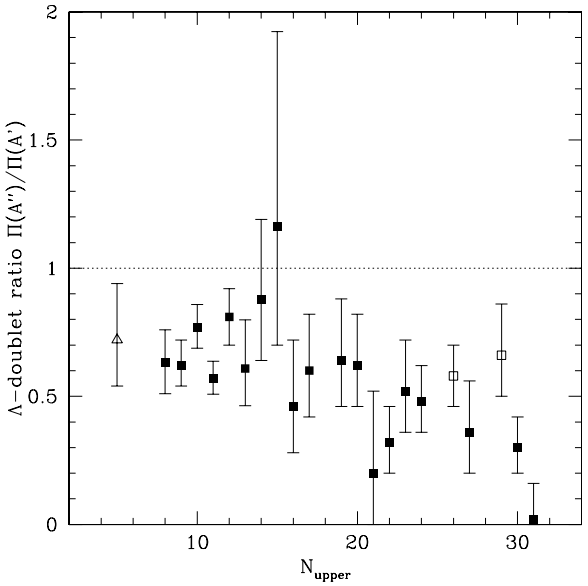

Figure 5. Ratio of the Λ-doublet population, $\Pi(A'')/\Pi(A')$, plotted against the upper rotational level N. The ratios were derived assuming that the OH emission is optically thin. A weighted average of ratios from the two rotational ladders is plotted for $N = 8$–13. The open triangle is for the cross-ladder transition, $^2\Pi_{1/2}$–$^2\Pi_{3/2}$ R3.5. The open squares indicate OH features for which the ratio could be skewed by a blue wing to the emission.

rotational temperatures are found for optically thin fits to the longer wavelength OH transitions of other CTTS (Salyk et al. 2011). Hence, the range in rotational temperature shown in detail in Figure 6 is not unique to DG Tau but appears to be a common characteristic of rotational OH emission from classical T Tauri stars (see also Figure 9 of Banzatti et al. 2012).

A rotation diagram with the cross-ladder transitions included is shown as an inset to Figure 6. A linear fit to solely the cross-ladder transitions (dotted line) corresponds to a temperature of 220 K. The inset also shows an optically thick fit (dashed line) to the cross-ladder transitions and the four lowest energy main-ladder transitions. The parameters are $T = 400$ K, $N(\mathrm{OH}) = 1 \times 10^{17}$ cm^{-2}, and a radius of 5.2 AU for the projected emitting area, although the fit is not particularly good (reduced $\chi^2 = 10.1$). The OH column density and temperature are comparable to those derived for other stars when cross-ladder transitions are included in the analysis (Carr & Najita 2008; Banzatti et al. 2012).

The fits shown in Figure 6 are meant to characterize the excitation of the emission rather than to argue for particular kinetic temperatures for the gas. The temperatures that come from fits to the lower rotational lines are indeed within the range of temperatures for other molecules found from LTE fits (CN11; Salyk et al. 2011), but no single combination of temperature and OH column density can fit all of the lower rotational main-ladder and cross-ladder transitions. It cannot be ruled out that the rotational diagram at these lower energies could be explained by

Table 2
OH Λ-doublet Population Ratios

λ (μm)	N_{up}	$\Pi(A'')/\Pi(A')$	OH Transitions
10.60	31	0.02 ± 0.14/0.02	3/2 R30.5ef, 1/2 R29.5f
10.82	30	0.30 ± 0.12/0.10	3/2 R29.5ef, 1/2 R28.5f
11.06	29	0.66 ± 0.20/0.16[a]	3/2 R28.5ef, 1/2 R27.5f
11.60	27	0.36 ± 0.20/0.16	3/2 R26.5ef, 1/2 R25.5f
11.92	26	0.58 ± 0.12/0.12[a]	3/2 R25.5ef, 1/2 R24.5f
12.65	24	0.48 ± 0.14/0.12	3/2 R23.5ef, 1/2 R22.5f
13.08	23	0.52 ± 0.20/0.16	3/2 R22.5ef, 1/2 R21.5f
13.54	22	0.32 ± 0.14/0.12	3/2 R21.5ef, 1/2 R20.5f
14.06	21	0.20 ± 0.32/0.20	3/2 R20.5ef, 1/2 R19.5ef
14.64	20	0.62 ± 0.20/0.16	3/2 R19.5ef, 1/2 R18.5ef
15.29	19	0.64 ± 0.24/0.18	3/2 R18.5ef, 1/2 R17.5ef
16.02	18	1.79 ± 0.60/0.43[b]	3/2 R17.5ef, 1/2 R16.5ef
16.84	17	0.60 ± 0.22/0.18	3/2 R16.5ef, 1/2 R15.5ef
17.77	16	0.46 ± 0.26/0.18	3/2 R15.5ef, 1/2 R14.5ef
18.84	15	1.16 ± 0.76/0.46	3/2 R14.5ef, 1/2 R13.5ef
20.06	14	0.88 ± 0.31/0.24	3/2 R13.5ef, 1/2 R12.5ef
21.44	13	0.58 ± 0.16/0.12	3/2 R12.5ef
21.53	13	0.74 ± 0.35/0.26	1/2 R11.5ef
23.10	12	0.72 ± 0.16/0.16	3/2 R11.5ef
23.22	12	0.88 ± 0.14/0.14	1/2 R10.5ef
25.06	11	0.58 ± 0.08/0.08	3/2 R10.5ef
25.24	11	0.56 ± 0.12/0.10	1/2 R9.5ef
27.42	10	0.66 ± 0.10/0.10	3/2 R9.5ef
27.67	10	1.11 ± 0.21/0.15	1/2 R8.5ef
30.31	9	0.50 ± 0.14/0.10	3/2 R8.5ef
30.68	9	0.92 ± 0.22/0.16	1/2 R7.5ef
33.91	8	0.64 ± 0.18/0.16	3/2 R7.5ef
34.48	8	0.62 ± 0.20/0.18	1/2 R6.5ef
24.63	5	0.72 ± 0.32/0.22	1/2–3/2 R3.5ef

Notes.
[a] Ratio could be skewed by blue wing to OH feature.
[b] Ratio could be skewed by potential H_2O emission.

thermal emission from multiple temperature and column density components. The rotational temperatures of the high-energy transitions, on the other hand, suggest a nonthermal origin. In Section 7, we will consider the assumption of thermalization of OH in light of the data on the Λ-doublet ratios and explore predictions for an OH cascade following OH formation via photodissociation or other processes.

6. WATER EMISSION IN DG Tau

Weak water emission features are present in the SH spectrum of DG Tau. In contrast, there is no clear detection of water emission in the LH spectrum, although there is a hint of the 33 μm feature (a blend of several H_2O lines). This conclusion about the presence of water emission differs from CN11, who reported an upper limit on the flux of the water lines at 17.1–17.4 μm. Figure 7 shows the 13–18 μm spectrum for DG Tau after subtraction of the model fits to the OH features (Section 4). There are a number of wavelength coincidences with water emission features, with the clearest ones at 15.18, 15.56, 15.8, and 17.22 μm.

The water spectrum for DG Tau is unlike those of the typical CTTS. A comparison shows that the relative line fluxes are different, including the absence of some lines normally seen in CTTS. In addition, water emission should have been detected in the LH spectrum, if DG Tau had the same ratio of emission in the LH relative to the SH as most CTTS. Synthetic LTE spectra for a range of temperatures were calculated for comparison to the DG

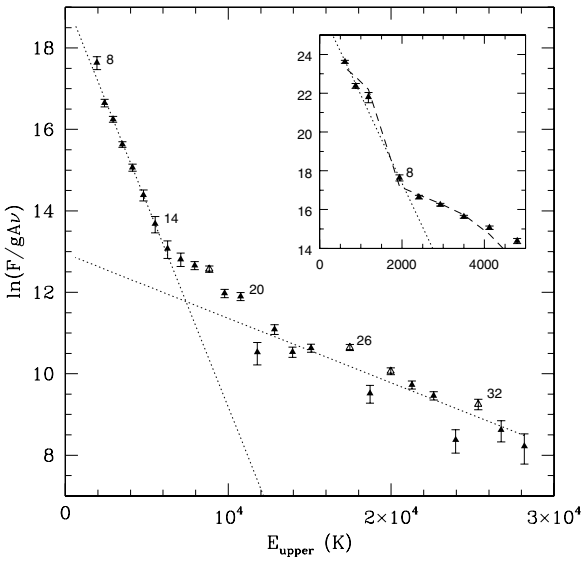

Figure 6. Rotational diagram for the OH emission from DG Tau. For reference, the upper rotational number N is labeled for some points. The linear fit to the high-energy points ($N > 20$) corresponds to a rotational temperature of 6300 K. The linear fit to the low-energy points ($N < 16$) corresponds to a rotational temperature of 1000 K. The open triangles mark OH features that may have other species contributing to the measured flux. (Inset) Rotational diagram for OH that includes the lower energy cross-ladder transitions. The linear fit to the three cross-ladder transitions (dotted line) corresponds to a rotational temperature of 220 K. The dashed line is an optically thick fit to the cross-ladder transitions plus the four lowest energy main-ladder transitions (N = 8–11); the model parameters are $T = 400$ K, $N(OH) = 1 \times 10^{17}$ cm^{-2}, and a radius for the projected emitting area of 5.2 AU.

Tau spectrum. While a best fit is precluded by the low S/N ratio of the water lines, it was found that $T > 900$ K, and $N(H_2O) > 5 \times 10^{17}$ but less than $\sim 10^{19}$ cm^{-2}, are required to reproduce the line ratios in the SH spectrum. The lower limit on the water column density requires the projected radius of the emitting area to be <0.5 AU for 1000 K. A model with $T = 1000$ K is compared to the DG Tau spectrum in Figure 7. This model explains the prominence of water features such as 15.18 and 15.56 μm and predicts line fluxes in the LH spectrum consistent with the nondetection of water emission at those wavelengths.

The required temperatures are significantly larger than the ~600 K found for the mid-infrared emission from CTTS in CN11, although the column densities are roughly similar. Both the temperature and column density are similar to values derived from 3 μm spectra of water emission in two T Tauri stars (Salyk et al. 2008), although the emission from these two stars has a larger radii extent of ~3 AU. Hot water emission at ~1500 K is measured in the K- and L-band spectra of other energetic young stars (SVS-13: Carr et al. 2004; V1331 Cyg: Doppmann et al. 2011), but this emission comes from a compact region with a H_2O column density of $\sim 10^{21}$ cm^{-2}. The latter results suggest that the near-infrared (2 μm) water emission reported for DG Tau (Najita et al. 2000) might be associated with a region that is more compact and denser than that from which the mid-infrared emission arises. In comparison, the recently reported far-infrared emission from warm water in DG Tau (Podio et al. 2013) originates from radii out to 90 AU from the star, orders of magnitude more extended than the mid-infrared water emission.

7. THE OH STATE POPULATIONS IN DG Tau

The rotational and Λ-doublet population derived for DG Tau are clues in understanding the origin and excitation of the

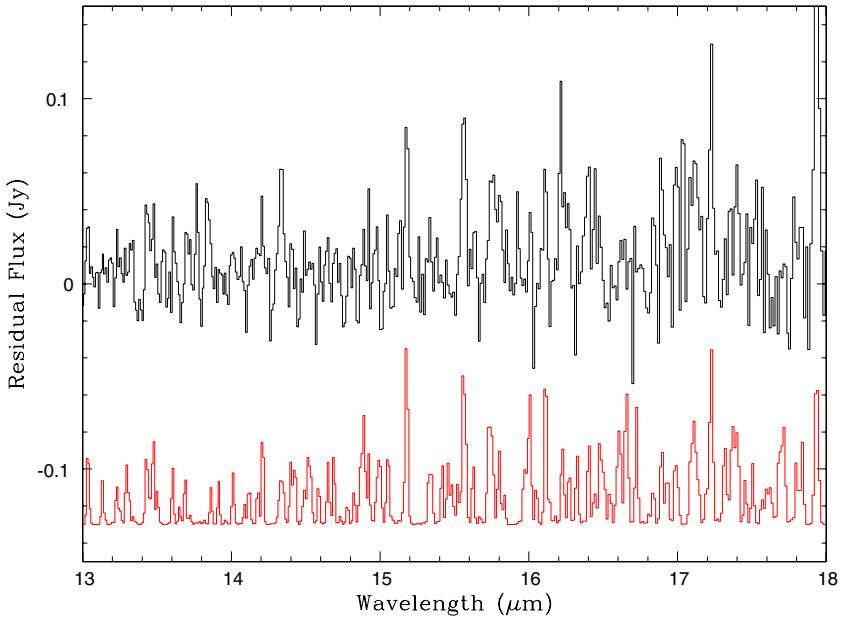

Figure 7. Water emission from DG Tau. The observed spectrum (upper) after subtraction of the continuum and a model fit to the OH features. A model water spectrum (lower) with $T = 1000$ K and $N(\mathrm{OH}) = 10^{18}$ cm^{-2}.

(A color version of this figure is available in the online journal.)

OH population. In this section, we focus on comparing the OH results for DG Tau with some processes that produce OH with a nonthermal distribution in the rotational and vibrational levels or unequal populations in the Λ-doublet states. While the lower rotational transitions could be excited by collisions, either in whole or in part, the large rotational temperatures of the high level transitions suggest the role of other processes. The following subsections draw upon laboratory and theoretical results in the literature relevant to the state populations of OH produced by photodissociation of H_2O and the reaction $O(^1D) + H_2$. This background material is summarized in greater detail in the Appendix. The Appendix also considers the critical densities for collisional excitation of OH and the effect of collisions on the Λ-doublet populations.

The photodissociation of water is an obvious candidate for the production of OH, given that CTTS have high levels of FUV radiation and an abundance of water in the atmospheres of the inner disks. As described in the Appendix, the OH product states differ depending on whether the photodissociating photons are in the first absorption band (FAB) or second absorption band (SAB) of water. For the FAB (∼1450–1900 Å), a majority of the excess energy goes into translation of the products, producing OH with rotational temperatures < 1000 K. In contrast, OH produced from photodissociation in the SAB (∼1150–1400 Å) has very high rotational excitation, peaking at $N \sim 45$ for OH in the $X^2\Pi$ ground electronic state. Another pathway for producing rotationally excited OH is the reaction of excited oxygen atoms in the ^1D state with H_2, with distributions that peak near $N = 25$ for the ground vibrational state. These three processes can also produce OH with a propensity for one of the two Λ-doublet states. OH from both photodissociation in the SAB and the reaction $O(^1D) + H_2$ are expected to show a preference for the $\Pi(A')$ state, whereas photodissociation in the FAB produces OH with either a preference for $\Pi(A'')$ or no preference. These processes are not expected to produce a preference for either of the spin–orbit ladders, and our measured ratios for the spin states (Figure 3(b)) are consistent with this.

Once OH molecules are produced by one of the mechanisms listed above, subsequent radiative transitions will preserve any original Λ-doublet preference that the molecules are formed with, although collisional transitions could modify or eliminate asymmetry in the population (see Appendix (A.4)). The selection rules for the radiative transitions are $e \rightarrow e$ and $f \rightarrow f$ for $\Delta J = 1$, and $e \leftrightarrow f$ for $\Delta J = 0$ (Brown et al. 1975). Hence, the Λ-doublet state is unchanged for the rotational transitions within a given ladder. The R- and P-branch cross-ladder transitions do change the Λ-doublet state; however, these will not produce a significant redistribution of the Λ-doublet population, because the probabilities for these transitions are orders of magnitude smaller than the main-ladder transitions.

One significance of the observed nonstatistical Λ-doublet ratios is that the OH population is not in thermal equilibrium. Because the Λ-doublet levels for a given rotational and spin–orbit state have the same statistical weight and virtually the same energy, they will have equal populations when in thermodynamic equilibrium. Hence, the measured preference for one Λ-doublet state shows that OH is not in LTE, even at the lowest observed rotational levels ($N = 8$) where thermalization of the rotational population would first occur. This result may not be surprising, given the relatively high critical densities for collisional excitation of OH. In Appendix A.4, we estimated that the critical densities for collisions with H_2 ranged from 2×10^{11} to 3×10^{12} cm^{-3} for $N = 10$–30, indicating that the density of the OH emission region is less than $\sim 10^{11}$ cm^{-3}. In some earlier analyses of *Spitzer* spectra of T Tauri stars, LTE has been assumed in order to derive OH rotational temperatures and column densities from the low rotational transitions (CN08; Salyk et al. 2011; Banzatti et al. 2012). It has also been suggested that the high rotational lines (in the SH module of the IRS) are due to prompt OH emission following photodissociation of water, while the rotationally cool component (observed in the LH module) represents OH molecules that have been thermally relaxed to the temperature of the surrounding gas (Najita et al. 2010; CN11). If the OH Λ-doublets in other T Tauri stars have nonstatistical

population ratios as observed for DG Tau, then the assumption of LTE is not valid, and the OH temperatures and column densities will need to be re-examined.

7.1. OH Formation via Photodissociation

Of the two main water absorption bands, photodissociation in the FAB is inconsistent with being the source of the bulk of the OH emission observed in the *Spitzer* spectrum of DG Tau. Because photodissociation in the FAB produces OH(X) with a relatively low rotational excitation, it is unable to account for the high rotational transitions (see the Appendix). For gas at 300 K, the OH products have rotational temperatures < 1000 K. At the higher temperatures expected for H_2O in DG Tau, the OH(X) rotational distribution is anticipated to be somewhat hotter. It is possible that the FAB could contribute to the lowest rotational lines observed in the IRS spectra. However, photodissociation in the FAB is expected to produce a preference, if any, for the $\Pi(A'')$ state. Therefore, the observed preference for the $\Pi(A')$ state argues against a major contribution to the OH population from photodissociation in the FAB, at least down to $N = 8$.

On the other hand, the observed $\Pi(A')$ preference, and the average OH(A'')/OH(A') ratio of 0.5, are in qualitative agreement with photodissociation of water in the SAB. While there are no laboratory measurements of the Λ-doublet ratio, theoretical results (Appendix A.2) suggest a OH(A'')/OH(A') ratio of 0.15–0.45 for photodissociation of water at approximately room temperature. This ratio is expected to increase at higher temperatures, as increased Coriolis coupling of the $\tilde{B}$–$\tilde{A}$ states increases the population in the $\Pi(A'')$ state, although the probability of the $\tilde{B}$–$\tilde{A}$ transition will quickly reach a limit above the first few rotational states (Dixon 1985).

In general, a dominance of the SAB in the photodissociation of water in CTTS should not be surprising given the known FUV spectra of CTTS. Lyα dominates the FUV flux (1150–1700 Å) in most CTTS systems, accounting for approximately 80% of the total FUV luminosity (Schindhelm et al. 2012b), although the fraction incident on the molecular disk gas may be less due to H I absorption between the star and disk. Therefore, the OH produced by photodissociation of water in CTTS should largely reflect the characteristics of photodissociation in the SAB[4]. Considering *only the FUV continuum*, the FUV data indicate that photodissociation in the FAB would dominate that in the SAB (Yang et al 2012; France et al 2011b, 2012). Assuming that the FUV spectrum of DF Tau (France et al. 2011b) is typical of CTTS, we estimate that six times more ionizing photons are available from the continuum within the FAB versus the SAB. Therefore, radiation in the FAB should contribute to the lower rotational levels of OH produced by photodissociation to some extent, depending on the dominance of Lyα in a particular star.

As summarized in Appendix A.2, the OH(X) rotational distribution peaks at $N \sim 45$ for photodissociation in the SAB. While the IRS spectra do not sample rotational levels this high, the observed distribution is falling with increasing N up to $N = 34$, unlike the experimental and theoretical results. A direct comparison with distributions measured in the laboratory is of limited value, however, because the astrophysical OH spectra do not sample the instantaneous distribution in which OH is formed, as the experiments are designed to do. The Einstein A-coefficients at $N = 45$ are ~ 600 s^{-1}, and hence the OH molecules will rapidly decay down the rotational ladder.

In order to explore whether the observed rotational distribution is consistent with OH formed by photodissociation in the SAB, we solved the equations of statistical equilibrium for a pure radiative cascade. It is assumed that the transitions are optically thin, that collisions are insignificant, and that only downward radiative transitions are important. These assumptions may be reasonable for the high rotational lines, where the lines are weak and the transition probabilities are high. Based on the estimates of the critical densities in Appendix A.3, collisions will be negligible for $N > 20$ for densities $< 10^{11}$ cm^{-3}. However, the detection of low N cross-ladder transitions suggests that the lowest observed rotational lines are optically thick; furthermore, the lower A-values (~ 20 s^{-1} at $N = 10$) increase the possibility that collisions could play a role for these lines.

In the model, OH molecules are formed at a given rate with specified vibrational and rotational distributions appropriate for dissociation by Lyα. The OH molecules are assumed to be destroyed at the same rate they are formed, with the destruction rate in a given state proportional to its steady-state population. By normalizing the rate equations by the volume density of OH, the single input parameter is the OH formation rate per OH molecule. Both the vibrational and rotational distributions were taken from Harich et al. (2000); for simplicity, the OH(X, $v = 0$) rotational distribution was used for all vibrational levels. Only the ground electronic state was considered, since approximately 80% of OH is formed in OH(X). Rotational levels up to $N = 48$ and vibrational levels up to $v = 9$ were included, with both fundamental and overtone transitions between vibrational levels. However, we found that inclusion of the excited vibrational levels made only a small change in the shape of the model rotational diagram compared to a model with solely the ground vibrational state. The Einstein A-coefficients were taken from the calculations of van der Loo & Groenenboom (2007), since these extend to higher rotational levels than those in the HITEMP database (Rothman et al. 2010). These A-coefficients are sufficient for the ground vibrational state, but extrapolation to higher rotational levels was required for excited vibrational states. The extrapolation is minor for the first few vibrational levels but becomes increasingly uncertain with v; for example, the calculations extend up to $N = 38$ for $v = 4$, and only to $N = 28$ for $v = 9$. Fortunately, the highest vibrational states have little impact on the results, but all of the ro-vibrational levels were retained for completeness.

The results for the cascade model are compared to the observed rotation diagram in Figure 8. Model curves are shown for OH formation rates per OH molecule of 0.1, 1.0 and 10 s^{-1}. The curves are identical for rates $\leqslant 0.1$ s^{-1}. The models were normalized to the observational rotation diagram at 25,000 K. The model shows that a radiative cascade from an initial rotation-vibrational distribution produced by photodissociation in the SAB does a reasonable job in reproducing the shape of the rotational diagram for energies greater than $\sim$10,000 K. At lower energies, the cascade model shows a continuous range in slope and a steep rise at low N, as the data do, but greatly under predicts the strength of the lower N transitions. Qualitatively, this might be explained if the lower N transitions are optically thick, since radiative trapping (reduced escape probability) would increase

[4] Strictly speaking, most of the photons at the wavelength of Lyα are likely to excite the $\tilde{D}$ state rather than the $\tilde{B}$ state responsible for the broad continuum absorption in the SAB. However, the $\tilde{D}$ state undergoes a fast nonadiabatic conversion to the $\tilde{B}$ state, and hence the dynamics of the photodissociation are determined by the $\tilde{B}$ surface (Fillion et al. 2001; Yuan et al. 2009). This is confirmed experimentally by the close similarity of the OH product state distribution for photodissociation by photons centered on the $\tilde{D}$ band and those at nearby wavelengths in the $\tilde{B}$ continuum.

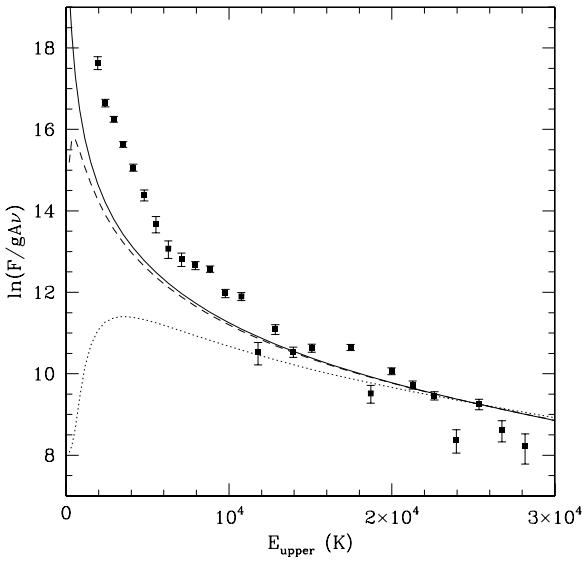

Figure 8. Radiative cascade model for OH compared to the observed rotational diagram. In the cascade model, OH is formed in high rotational states with the measured ro-vibrational distribution for dissociation by Lyα (see text, Section 7.1). Only downward radiative transitions are considered. Models are shown for OH formation rates per OH molecule of 0.1 (solid curve), 1.0 (dashed curve) and 10 s^{-1} (dotted curve). The curves are all normalized to the observed rotational diagram at 25,000 K.

the population in these levels. A radiative transfer calculation is needed to investigate this idea. Alternatively, other processes or emission from a cool thermal OH component could contribute to the emission at lower N. Regardless of the exact explanation for the low N lines, the population distribution of the high rotational lines can be understood as a radiative cascade of OH following its formation by photodissociation of H_2O in the SAB, as long as the formation rates are $\sim$1 s^{-1} or less.

An order of magnitude estimate for the rate of photodissociating photons (and the OH formation rate) for a typical CTTS can be determined for the case where the H_2O and OH are in a disk. From Schindhelm et al. (2012b), the average Lyα luminosity that is incident on the H_2 is about 0.006 $L_\odot$. Taking 0.5 AU as a typical radius for disk molecular emission in the mid-infrared (CN11; Salyk et al. 2011), this corresponds to 2×10^{15} photons s^{-1} cm^{-2}. The water photodissocation cross-section per H_2O molecule is 1.3×10^{-17} cm^2 at Lyα. Furthermore, about 65% of water photodissociated in the SAB produces OH(X). This leads to an OH formation rate per H_2O molecule of 0.02 s^{-1}. This rate will decrease into the disk atmosphere as the FUV is attenuated. The accretion rate for DG Tau is significantly higher than an average CTTS; hence, the photodissocation rate could be an order of magnitude higher for DG Tau. This suggests an OH formation rate per H_2O molecule $\sim$0.1 s^{-1} near the top of the molecule layer.

Because this estimate of the OH formation rate is per H_2O molecule, and the formation rate in the cascade model is per OH molecule, the ratio of the H_2O to OH abundance is needed to compare these rates. Models that consider the photodissociation of water and OH in the disk atmosphere can provide some guidance on the H_2O to OH ratio. In the simple model used in Bethell & Bergin (2009), the H_2O/OH ratio is $\sim$0.5 near the top of the molecular photodissociation region. The ratio increases to $\sim$5 at the bottom of the photodissociation layer, but this is balanced by a factor of $\sim$5 attenuation in the dissociating photons. Similar results are found in more detailed modeling by Ádámkovics et al. (2014). The H_2O/OH ratio is $\sim$unity at the top of the molecular photodissociation region for their standard model at 1 AU. The ratio increases to $\sim$5 near the bottom of the photodissociation layer, with a factor of five attenuation of the FUV. Given the above OH formation rate per H_2O molecule of $\sim$0.1 s^{-1}, this implies an equivalent formation rate of OH per OH molecule $<$0.1 s^{-1}, well below the 1 s^{-1} required by the cascade model. Hence, plausible H_2O dissociation rates for DG Tau are sufficiently low to explain the population distribution of high rotational OH lines as a cascade from the highly excited states expected for photodissociation of water by Lyα.

7.2. OH Formation via O(^1D) + H_2

The excited state of oxygen in the reaction O(^1D) + H_2 is the upper level of the [O I] 6300 Å line. This is a prominent emission line in all CTTS (e.g., Hartigan et al. 1995). In general, both high-velocity and low-velocity components are observed. The high-velocity component originates in a dense stellar jet. The origin of the low-velocity component is less clear, but it could originate in slow disk wind. In the case of DG Tau, the [O I] 6300 Å line is dominated by high-velocity blueshifted emission.

The O(^1D) + H_2 reaction was suggested in the context of TW Hya as a possible alternate or supplement to photodissoction of H_2O for producing the highly excited OH emission in that star (Gorti et al. 2011). As they proposed for TW Hya, the excited oxygen atoms result from photodissociation of OH, which produces oxygen in the ^1D state about 50% of the time (in general, O(^1D) can also be thermally populated). OH is then readily re-formed in excited rotational states via the O(^1D) + H_2 reaction. The competition between O(^1D) reacting with H_2 to form OH, and radiative decay to produce 6300 Å emission, depends on density, with the former dominating at gas densities $>10^7$ cm^{-3} (Gorti et al 2011).

The above reaction cannot explain the highest OH rotational levels observed in DG Tau, because the rotational distribution peaks at $N = 25$ for the ground vibrational state and rotational levels above $N = 30$ are not populated (Liu et al. 2000). The reaction does, however, produce OH(X) with the same preference for the $\Pi(A')$ Λ-doublet state as was found for DG Tau. A contribution to the OH population at $N < 25$, therefore, is not readily ruled out.

In order to compare the observed rotational distribution with that expected for OH formed by the O(^1D) + H_2 reaction, the equations of statistical equilibrium were solved for a pure cascade as was done for photodissociation in the SAB. The initial rotational and vibrational state distributions were taken from the experimental results of Liu et al. (2000). It was also possible to calculate the Λ-doublet ratio as a function of N by using the experimental and theoretical data for the initial Λ-doublet population as a function of rotational and vibrational level (Cleveland et al. 1987; Mikulecky & Gericke 1992; Alexander et al. 2004).

Results for the rotational population are compared to the observed rotational diagram in Figure 9(a), for OH formation rates per OH molecule of 0.1 and 10 s^{-1}. In this case, the models were normalized to the data at 7000 K to examine the potential of explaining the data at low to intermediate N. The results suggest that if the total OH produced by the O(^1D) + H_2 reaction is sufficiently large, then it could account for some, or a majority, of the OH population at lower N.

The results for the Λ-doublet ratio are shown in Figure 9(b) for the same OH formation rates. At high N, the $\Pi(A'')/\Pi(A')$ ratio is dominated by the ratio at the peaks of the rotational

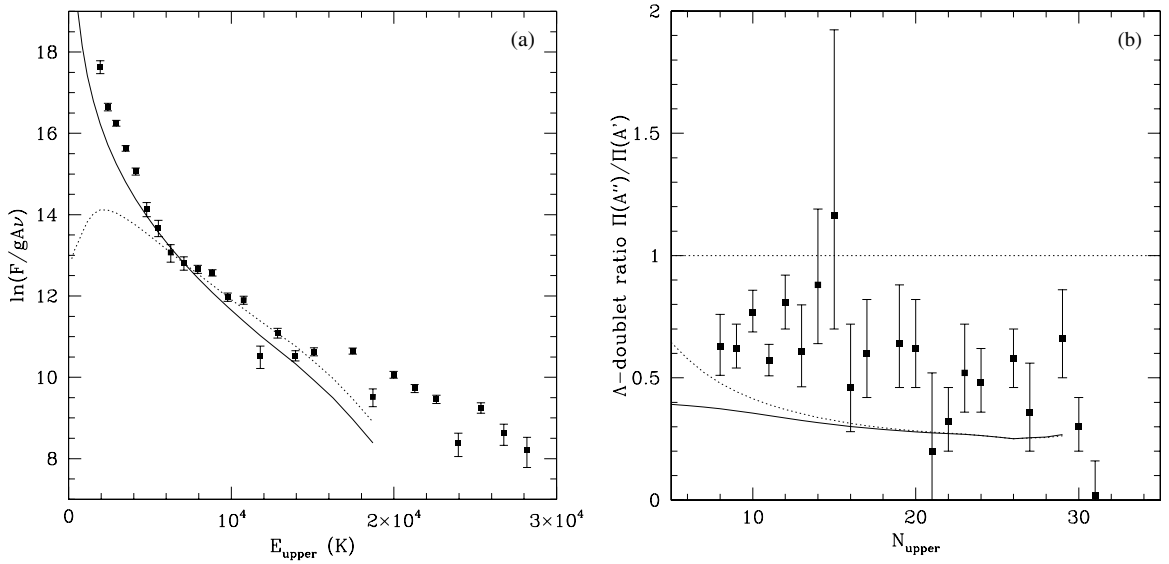

Figure 9. (a) Radiative cascade model, as in Figure 8, but for an initial ro-vibrational distribution appropriate for OH formed by the reaction O(^1D) + H_2 (see Section 7.2). Models are shown for OH formation rates per OH molecule of 0.1 (solid curve) and 10 s^{-1} (dotted curve). The curves are normalized to the observed rotational diagram at 7000 K. (b) The Λ-doublet ratio as a function of upper level *N* predicted by the cascade model is compared to the measured values, for the same OH formation rates in (a).

distributions, which is ∼0.25. At low *N* and at sufficiently low formation rate (e.g., 0.1 s^{-1}), the ratio converges to the average ratio for the total ro-vibrational population, which is ∼0.4. These predicted $\Pi(A'')/\Pi(A')$ ratios are significantly lower than the observed ratios.

8. DISCUSSION

8.1. Photodissociation of H_2O

The high rotational lines of OH ($N_{up} > 20$) observed in DG Tau provide evidence for the photodissociation of H_2O by FUV photons in the second absorption band of water. The slope of the observed rotational diagram for these rotational levels is consistent with that expected for a radiative cascade following formation of OH in very high ($N \sim 45$) rotational states by photodissociation of H_2O in the SAB. Other processes we have considered, photodissociation of H_2O in the FAB and formation of OH by the reaction of O(^1D) with H_2, do not populate the highest rotational levels that are observed. A thermal population would require temperatures ∼6000 K and densities $\sim 10^{12}$ cm^{-3}; furthermore, OH would be collisionally dissociated under these conditions. Ultraviolet pumping of OH could populate higher vibrational states; however, this mechanism cannot increase the rotational excitation, due to the rotational selection rules for the radiative transitions. The observed preference for the symmetric A' state of the Λ-doublet levels provides additional support for OH formed by photodissociation of water in the SAB. While there are no laboratory measurements of the Λ-doublet ratio for this process, the observed $\Pi(A'')/\Pi(A')$ ratio of ∼0.4 for $N >$ 20 is a plausible value based on theoretical calculations.

The presence of water in DG Tau is well demonstrated by H_2O emission in the near-infrared (Najita et al. 2000), mid-infrared (this paper), and the far-infrared (Podio et al. 2012; 2013; Fedele et al. 2013), which together suggest that water is present from the inner to the outer disk. However, the mid-infrared spectrum of DG Tau has a high ratio of OH to H_2O emission line fluxes (Carr & Najita 2011), in sharp contrast to the majority of CTTS. This could be a direct result of the high FUV luminosity of DG Tau, since the column density of OH relative to H_2O is predicted to increase with increasing FUV flux (Bethell & Bergin 2009; Ádámkovics et al. 2014). Interestingly, Podio et al. (2013) suggest that the high UV flux is responsible for the strong ground-state transitions of H_2O in DG Tau, due the increased heating of the surface layers of the outer disk.

The OH emission spectra observed for other CTTS are similar to that of DG Tau: high rotational lines of OH indicating rotational temperatures of thousands K, along with lower OH rotational lines with rotational temperatures of several hundred K (Carr & Najita 2008; Najita et al. 2010; CN11; Salyk et al. 2011; Banzatti et al. 2012). While those spectra have not been analyzed in the detail presented here, the results for DG Tau lend further support to previous suggestions (Najita et al. 2010; CN11) that the high-rotational OH emission is the result of photodissociation of water. It is reasonable to conclude that the photodissociation of water by FUV radiation is likely to be an active process in the surface disk layers of CTTS. More direct evidence for FUV irradiation of warm molecular gas comes from recent observations of fluorescent emission from CO and H_2 excited by Lyα photons (France et al. 2011a, 2012; Schindhelm et al. 2012a). The measured excitation temperatures and column densities of the Lyα excited CO gas (Schindhelm et al. 2012a) are comparable to those of the warm H_2O gas derived from mid-infrared spectra. This same Lyα radiation is available for photodissociation of water and production of rotationally hot OH.

The evidence that photodissociation of water is occurring is relevant to two related processes that may be of importance in the disk atmosphere. One is the role of water in heating the molecular gas layer by absorption of FUV photons. The energy deposited into the gas by the photodissociation of water is potentially a significant heating source in the upper molecular atmosphere of the disk (Bethell & Bergin 2009; Najita et al. 2011; Ádámkovics et al. 2014). The other is the ability of water to self-shield. In the situation where dust opacity in the upper atmosphere is significantly reduced, water can shield molecular gas lower in the disk atmosphere from photodissociating FUV radiation. The measured column densities for warm water (CN11; Salyk et al. 2011) are more than sufficient for strong

shielding over the wavelength range of the water absorption bands (Bethell & Bergin 2009).

8.2. The Lower Rotational OH Population

The process responsible for the population in the lower rotational levels ($N = 8$–20) is less clear. The cascade from higher OH rotational states will produce a substantial population in these levels, but the optically thin model does not produce sufficient population in the lower levels to match the rotational diagram (Figure 8). Line trapping can increase the level populations as lines become optically thick, but a radiative transfer calculation is required to determine whether the cascade could fully account for the OH population in these levels.

The reason for the apparent increase in the Λ-doublet ratio, from ∼0.4 at high N to ∼0.7 at low N, is not clear. In the cascade model, the $\Pi(A'')/\Pi(A')$ ratio of 0.4 at high N should represent the average Λ-doublet ratio with which the OH population was formed, since this ratio will not be altered in a pure radiative cascade. Recall that the derivation of the Λ-doublet ratios assumes that the lines are optically thin. If lines are optically thick, then the derived ratios will be larger than the actual values. Hence, an increase in the Λ-doublet ratio at lower N could simply be a result of the lines becoming optically thick. Measurements of the Λ-doublet ratio for cross-ladder lines, which are more likely to be optically thin, could clarify the values of the intrinsic ratio. The cross-ladder line in Figure 5 has a ratio similar to the low-N main-ladder lines, suggesting that optical depth cannot be the sole explanation; however, this is a single line, and the uncertainties are too large to be definitive.

An alternative is that collisions are significant enough at lower N to potentially alter the Λ-doublet population. The Λ-doublet ratio could be increased relative to an initial ratio ∼0.4, depending on the density relative to the critical density of the rotational level. If the density is equal to or greater than the critical density, then the Λ-doublet ratio will approach 1.0. If the density is far below the critical density, then radiative transitions will completely dominate. Hence, there will be a restricted density range for each rotational level where collisions could affect the Λ-doublet ratio but not produce LTE. We estimated critical densities of 10^{11}–10^{12} cm^{-3} for the rotational levels $N = 10$–20, while $N_{\rm crit} \sim 10^{10}$ cm^{-3} at $N = 5$, the rotational level of the cross-ladder line in Figure 5. Given this two order of magnitude range in critical density between $N = 5$ and 20, it appears doubtful that collisions could produce the approximately constant Λ-doublet ratio over this range. However, quantitative estimates of the effect of collisions on the Λ-doublet population will require collisional rates for higher rotational levels than are currently available.

An additional possibility is that the observed Λ-doublet ratios at lower N reflect a blend of OH populations, with contributions from other processes along side the OH cascade from high rotational levels. A thermal population of OH at gas temperatures $\leqslant 1000$ K could contribute to the flux of the lower rotational OH lines and move the apparent Λ-doublet ratio closer to unity. An OH population formed by photodissociation of water in the FAB could have a similar effect. Neither of these processes, however, would be expected to contribute much at intermediate ($N \sim 18$) rotational levels. We have shown how the reaction of oxygen in the excited ^1D state with H_2 could contribute to the OH population at low and intermediate N. Since this process produces OH with $\Pi(A'')/\Pi(A')$ ratios ∼0.3 (Figure 9(b)), optical depth effects or collisions would have to be invoked to increase the Λ-doublet ratio, as discussed above.

DG Tau also shows emission from the lowest rotational OH transitions ($N_{\rm up} = 2$–5) observed in the far-infrared with the PACS instrument on the *Herschel* Space Observatory (Fedele et al. 2013). A LTE fit to these OH lines gave $T = 115$ K, $N(\mathrm{OH}) = 4 \times 10^{15}$ cm^{-2}, and 50 AU for the radius of the emitting area. The optically thick solution is driven by the measurement of the 79 μm cross-ladder line. The two lowest energy cross-ladder transitions measured in the mid-infrared (Table 1) share the upper energy level of two of the main-ladder lines in the PACS spectrum. The comparable fluxes in these main and cross-ladder lines confirm that the OH lines are optically thick up to at least $N_{\rm up} = 5$. Fedele et al. suggest a contribution to the OH emission from shocks in an associated outflow, based on the large areal extent from the LTE fit. However, the double-peaked emission profiles of the ground-state H_2O transitions measured with *Herschel*/HIFI (Podio et al. 2013) indicate disk emission out to ∼90 AU, and a similar radial extent for far-infrared OH disk emission is conceivable.

8.3. The Λ-doublet Ratio in Comets

Another astronomical case of Λ-doubling components measured for rotationally excited OH is the study of OH prompt emission in two comets by Bonev & Mumma (2006). For comets, the photodissociation of H_2O and subsequent OH emission occur under physical conditions and a radiation field that are different from the situation for T Tauri stars; hence, differences in the state populations of OH should be expected. Their measurements are from high-resolution spectra in the OH fundamental ro-vibrational transitions near 3.3 μm. Bonev & Mumma show that the Λ-doublet ratio in the $v = 1$ level decreases with increasing rotational level, from ∼1.4 at $N = 3$ to ∼0.3 at $N = 16$. Hence, the $\Pi(A'')$ state is favored at low N, while the $\Pi(A')$ dominates at high N, rather unlike the Λ-doublet distribution for DG Tau. They reach no definite conclusion about this distribution of the Λ-doublet population, but they note that the decreasing ratio for $J' > 8.5$ agrees with measurements for the reaction $O(^1D) + H_2$. We point out that this would make OH a less direct proxy for water, because the $O(^1D)$ must first be formed by photodissociation of H_2O, and $O(^1D)$ can also result from the photodissociation of OH and other molecules. The photodissociation of water in comets has similar rates in the FAB and SAB, with Lyα accounting for most of the SAB (Crovisier 1989; Wu & Chen 1993). We suggest that the measured trend in the Λ-doublet ratios might be due to a blend of OH cascades produced by photodissociation of water in the FAB and SAB, with the proportion varying with rotational level. In this scenario, the Λ-doublet ratio of ∼0.3 measured at $N = 16$ in these comets would represent the average ratio for OH produced by photodissociation in the SAB. We note that 0.3 is consistent with the ratio measured in DG Tau in the high N limit. A cascade model along the lines of the one used in this paper could be used to explore the viability of this explanation for the Λ-doublet ratios measured in these comets.

9. SUMMARY

We have analyzed the OH and H_2O emission from the very active T Tauri star DG Tau, using spectra obtained with the *Spitzer Space Telescope*. The rotational OH lines are observed in emission over the entire wavelength extent (10–35 μm) of the SH + LH modules of the IRS, covering upper energy levels of 1900–28,000 K, which correspond to upper state quantum numbers $N = 8$–34. OH emission from transitions between the

two spin–orbit rotational ladders (cross-ladder transitions) was also measured, with upper energy levels of 600–1190 K (N = 4–6). The strength of these cross-ladder transitions implies high optical depths in the lower rotational main-ladder transitions.

The *Spitzer* spectrum of DG Tau also shows weak H_2O emission lines. The rotational excitation of the H_2O, ∼1000 K, is higher than the typical ∼600 K temperature for the mid-infrared water emission in other CTTS. The weakness of the water emission in DG Tau with respect to the OH emission is also in contrast to the large majority of CTTS in which the H_2O emission dominates over OH emission. This may be due to the high FUV luminosity of DG Tau, resulting in an increase of the OH column density relative to H_2O.

The rotational diagram for OH shows a wide range in slope that cannot be fit with a single temperature–column density component, indicating a potential range of excitation conditions for OH. A linear fit to the highest energy transitions gives a rotational temperature of 6300 K. The lower energy main-ladder transitions can be characterized by rotational temperatures of ∼1000 K, while the low-energy cross-ladder transitions can be fit with $T \sim 200$ K.

The Λ-doublet components of the OH transitions are not equally populated in DG Tau. Based on fits to the observed blends of the OH spin–orbit and Λ-doublet components, as well as direct measurements for the lowest rotational levels, it was found that the Λ-doublet levels have a preference for the symmetric $\Pi(A')$ state at all rotational levels. The Λ-doublet population ratio of the $\Pi(A'')$ to $\Pi(A')$ states has an average value of 0.5. There is a slight trend with rotational level, increasing from ∼0.4 for $N > 20$ to ∼0.7 for $N < 15$. Because the ratios were derived assuming optically thin transitions, the intrinsic ratios would be lower for transitions that are optically thick. The nonstatistical Λ-doublet population also indicates that the rotational levels are not in thermal equilibrium, even in the lowest observed rotational states. This suggests that LTE determinations of temperature and column density from mid-infrared OH emission in CTTS should be viewed with caution. We estimate that the density of the OH emission region is less than $\sim 10^{11}$ cm^{-3}.

We examined different non-thermal processes that can produce rotationally excited OH with Λ-doublet asymmetries. The rotationally hot OH emission ($N > 20$) can be explained as an OH population that is formed from photodissociation of H_2O by FUV radiation in the second absorption band of water, including Lyα. This process produces a highly excited rotational OH population that peaks at $N \sim 45$. A simple cascade model is used to show that the rotational distribution observed above N of 20 is consistent with a pure radiative cascade from the highly excited states expected for photodissociation of water in the SAB. The required OH formation rates are consistent with our estimate of a plausible rate of photo-dissociating photons for DG Tau. The observed preference for the $\Pi(A')$ state of the Λ-doublet levels in DG Tau is also consistent with expectations for OH products from photodissociation of H_2O in the SAB.

Photodissociation of H_2O in the first absorption band (center ∼1650 Å) of water forms OH with far lower rotational excitation that cannot account for the OH emission at $N > 15$. In addition, this process does not produce OH with the observed preference for the $\Pi(A')$ state. This suggests that any contribution from photodissociation in the FAB to lower rotational levels does not dominate the observed OH population. Another potential process is the reaction $O(^1D) + H_2 \rightarrow OH + H$. This reaction produces OH with the observed preference for the $\Pi(A')$ state and a ro-vibrational distribution that could contribute to the observed OH emission below $N = 25$, but it cannot explain the higher rotational state population. More detailed modeling will be required to understand the OH population of the low and intermediate rotational states and, in particular, the relative contributions of: the OH cascade from photodissociation of H_2O in the SAB, photodissociation of H_2O in the FAB, the reaction of $O(^1D)$ with H_2, and a collisionally excited OH population. The lack of rate constants at these rotational levels for collisions of OH with H_2 and H is one hindrance to modeling the OH population and to evaluating the effect of collisions on the Λ-doublet asymmetries.

The analysis of the OH emission provides good evidence that photodissociation of water is taking place in DG Tau. As other mechanisms cannot produce the very high rotational OH emission, the detection of these transitions may serve as a signature of H_2O photodissociation in the SAB. Since rotationally hot OH emission is observed from most CTTS, the photodissociation of water is likely to be a common process in the molecular gas layer of T Tauri star disk atmospheres. This absorption of FUV radiation by water supports the suggested roles of water as a heating source in the gas atmosphere and as a mechanism to shield molecules at lower layers from photodissociating radiation.

This work is based on observations made with the *Spitzer Space Telescope*, which is operated by the Jet Propulsion Laboratory, California Institute of Technology under a contract with NASA. Support for this work was provided by NASA. Basic research in infrared astrophysics at the Naval Research Laboratory is supported by 6.1 base funding. J.N. gratefully acknowledges support from the Institute for Theory and Computation at the Harvard-Smithsonian Center for Astrophysics.

APPENDIX

EXPERIMENTAL AND THEORETICAL RESULTS ON STATE POPULATIONS OF OH

A.1. Photodissociation in the First Absorption Band

The first absorption band (FAB) of H_2O is a broad continuum feature from about 1450 to 1900 Å, peaking at ∼1650 Å. Photons within this band excite H_2O from the ground electronic state $\tilde{X}(^1A_1)$ to the $\tilde{A}(^1B_1)$ electronic state. The potential energy surface of the $\tilde{A}(^1B_1)$ state is purely repulsive, leading to direct dissociation of the parent water molecule, producing $OH(X^2\Pi)$ + H. The majority of the excess energy goes into translation of the products.

There is relatively little rotational excitation of the OH product. In experiments on the photodissociation of H_2O at 1570 Å, the OH rotational temperature is about 300 K for cold (∼10 K) water (Andresen et al. 1984). The rotational temperature of OH increases as the temperature of H_2O is increased, since the parent's thermal rotational energy is transferred to the OH product. At room temperature (300 K), the OH rotational temperature is close to 900 K, for both the ground and first excited vibrational levels. In the OH vibrational distribution, approximately one-third of the total population is in the ground vibrational state (Hwang et al. 1999; Yang et al. 2000), with a similar fraction in the first excited state ($v = 1$). The population then decreases with increasing vibrational level, with only ∼4% of the population in $v = 4$.

The OH population of the two Λ-doublet levels show a preference for asymmetric A'' state, at least for the case of cold H_2O. In an experiment at 1570 Å (Andresen et al. 1984), the $\Pi(A'')$ to $\Pi(A')$ ratio increases rapidly with N, from a ratio of 2 at $N = 1$ to 20 at $N = 9$ (the highest rotational level measured). However, for warm H_2O at or near room temperature, this Λ-doublet population inversion is greatly decreased or eliminated (Andresen et al. 1983; Andresen et al. 1984; Häusler et al. 1987; Grunewald et al. 1987). Depending on the experiment, the $\Pi(A'')/\Pi(A')$ ratio is found to be near unity, but no more than 2–3. In contrast to the Λ-doublet states, the spin–orbit distributions are found to be close to statistical in these experiments.

A.2. Photodissociation in the Second Absorption Band

Photodissociation in the second absorption band (SAB) of H_2O is more complex than in the FAB. This continuum absorption band (∼1150–1400 Å) has a maximum at 1280 Å and is associated with excitation of the ground electronic state of H_2O to the $\tilde{B}(^1A_1)$ electronic state. Direct dissociation on the $\tilde{B}$ surface leads to an H atom and electronically excited OH ($A^2\Sigma^+$). However, the majority of OH is formed in the ground electronic state ($X^2\Pi$) by indirect dissociation; the branching ratio of OH(A) to OH(X) is measured to be about 20% (Mordaunt et al. 1994; Harich et al. 2000; Cheng et al. 2011). There are two possible pathways to OH(X): transition from the $\tilde{B}$ to the $\tilde{X}$ state at the conical intersections of their potential energy surfaces, and crossing from $\tilde{B}$ to $\tilde{A}$ by Coriolis coupling between the two states. The strength of the later coupling is dependent on the rotational excitation of the H_2O molecule. Both the OH(A) and OH(X) products are formed with a much higher rotational excitation than OH from photodissociation in the FAB.

The OH(X) population shows a very high degree of rotational excitation, with a distribution that peaks near $N = 45$. Approximately half of the total OH(X) population is in the ground vibrational state, with the remainder distributed about evenly over $v = 1$ to $v = 9$. The rotational distribution in higher vibrational states peak at similar values of N, though they are more sharply peaked than at $v = 0$ (Mordaunt et al. 1994; Harich et al. 2000; Cheng et al. 2011).

The population ratio of lambda-doublets for OH(X) has not been directly measured, but some theoretical guidance is available (Mordaunt et al. 1994; Dixon 1995, 1999) along with some indirect experimental support. For H_2O in the ground rotational state, the only dissociation pathway to OH(X) products is through the conical intersection of the $\tilde{B}$ and $\tilde{X}$ potential energy surfaces. This pathway produces a OH(X) population that is almost exclusively in the A' Λ-doublet levels. For rotationally excited H_2O, however, Coriolis coupling between the $\tilde{B}$ and $\tilde{A}$ states becomes possible. This dissociation pathway mainly populates the A'' Λ-doublets and populates somewhat lower values of N. Comparisons between measured and calculated rotational distributions indicate that the $\tilde{B}$–$\tilde{X}$ conical intersection is the main dissociation pathway at the low H_2O temperatures used in the experiments, although the $\tilde{B}$–$\tilde{A}$ pathway still contributes, even at 10 K. Because the Coriolis coupling depends on the rotational state of H_2O, the importance of the $\tilde{B}$–$\tilde{A}$ channel is expected to increase with the rotational temperature of the parent H_2O molecules. This is supported by comparison of the OH(X) populations produced from photodissociation of H_2O at 10 K and 165 K (Hwang et al. 1999), in which the rotational distribution shifts to slightly lower N at the higher temperature, indicating enhancement of the $\tilde{B}$–$\tilde{A}$ Coriolis coupling. Comparison of the rotational distributions from Mordaunt et al. (1994) and Harich et al. (2000), recorded with H_2O rotational temperatures of ∼125 K and 10 K respectively, also shows an enhancement of lower N levels at the higher temperature. Mordaunt et al. (1994) calculate the branching ratio $OH(A'')/OH(A')$ to be 0.45 for a rotational state of H_2O roughly appropriate for room temperature. In a similar but later calculation by the same author, this ratio appears to be closer to 0.15 (Dixon 1995, Figure 1). The populations in the two spin–orbit states are expected to be close to equal (Dixon 1995).

The OH(A) population has a lower rotational excitation than OH(X). In general, the OH(A) rotational distribution increases with N, peaking near the highest energetically accessible rotational level and then dropping sharply. The peak of the rotational distribution, N_{peak}, decreases with increasing wavelength and with increasing vibrational level. For the ground vibrational state ($v = 0$), N_{peak} is about 22 for the wavelength of Lyα (1216 Å) and about 10 for 1330 Å photons; this decreases in $v = 1$ to $N_{peak} \sim 14$ and ∼3, respectively. Nearly all of the OH(A) is produced in the first two vibrational levels. The vibrational distribution has some dependence on wavelength: about 60% is found in $v = 0$ near the wavelength of Lyα, but more than 90% is in $v = 0$ near 1310 Å (Zanganeh et al 2000; Fillion et al. 2001).

A.3. The Reaction $O(^1D) + H_2$

Another pathway for producing rotationally excited OH is the reaction $O(^1D) + H_2$. This proceeds mainly via an insertion reaction that involves an intermediate excited H_2O complex which then dissociates, resulting in OH($X^2\Pi$) and an H atom. Within a vibrational level, the rotational population increases with N, reaches a maximum value near the most energetically allowed state, and then drops sharply. For the ground vibrational state, the peak is near $N = 25$. The peak value of N decreases monotonically as the vibrational level increases; for $v = 4$, the peak is near $N = 15$. The vibrational population also monotonically decreases with higher vibrational levels. Approximately 30% of the population is formed in $v = 0$, decreasing to about 8% in $v = 4$ (Smith & Butler 1980; Cleveland et al. 1987; Mikulecky & Gericke 1992; Liu, X. et al. 2000).

The reaction shows a strong propensity for producing OH in the $\Pi(A')$ Λ-doublet state (Butler et al. 1986; Cleveland et al. 1987; Mikulecky & Gericke 1992; Alexander et al. 2004). The ratio of $\Pi(A'')$ to $\Pi(A')$ decreases with rotational level. At low values of N, the ratio is near unity; at the peak of the rotational distribution within a given vibrational level, the ratio reaches values ∼0.25. The two spin–orbit levels are equally populated.

A.4. Collisions

Rate constants for the rotational excitation of OH by collisions with H_2 have been calculated for only the first five rotational states (Offer et al. 1994). Based on these rates, the critical densities range from 10^8 to 10^{10} cm^{-3} from the lowest to highest rotational level. In order to estimate critical densities for higher rotational states, some assumption is needed for the collisional rates. An examination of the calculated rates shows that the sum of the de-excitation rate constants from a rotational level decreases with increasing rotational state, roughly scaling inversely with N. However, we assume instead that the collisional rates remain constant at those for the highest calculated level, i.e., the critical density scales with the Einstein

A-coefficient. This assumption gives critical densities of 2×10^{11}, 10^{12}, and 3×10^{12} cm^{-3} for $N = 10$, 20 and 30, respectively. The density for thermal equilibrium could be an order of magnitude or more higher, depending on the line opacity. These densities will be higher if the rate constants continue to decrease with N. We conclude that even the lowest rotational levels observed in the IRS spectra are unlikely to be in LTE for densities below $\sim 10^{12}$ cm^{-3}.

When OH is not in thermal equilibrium, asymmetries between the Λ-doublet components can be produced by collisions with H_2, with a propensity for the $\Pi(A')$ levels. While this effect is most pronounced for para-H_2, it is also present when ortho-H_2 is included (Offer & van Dishoeck 1992). We used the non-LTE code RADEX (van der Tak et al. 2007) to explore the Λ-doublet ratio under collisional excitation, for an ortho:para ratio of 3:1 and the collision rate constants of Offer et al. (1994), which cover the first five rotational levels. In general, the OH(A'')/OH(A') ratio for a rotational transition is at least 0.9 when the H_2 density equals the critical density of the transition, when the main-ladder lines are not optically thick. In comparison, the excitation temperature is not equal to the same fraction of the kinetic temperature until the density is about an order of magnitude larger. Below the critical density, the Λ-doublet ratio decreases with decreasing density. As an example, at two orders of magnitude below the critical density for transitions out of $N = 4$, the ratio is ∼0.3 for $T = 400$ K and N(OH) = 10^{14} cm^{-2}; the ratio increases to ∼0.7 for a column density of 10^{16} cm^{-2} when the lines are very optically thick. In the absence of collision rates for the higher rotational transitions covered by the *Spitzer* IRS data, the behavior of the Λ-doublet ratios cannot be predicted, and we can only presume that qualitatively similar Λ-doublet asymmetries could be produced by collisions under the right conditions.

If the OH emission originates in a molecular photodissociation region, collisions with atomic hydrogen may dominate over collisions with H_2. Relatively less work exists for rotational excitation of OH by atomic H than by H_2. The best rate constants are the recent calculations by Atahan & Alexander (2006). Since they were concerned with Λ-doublet population inversions with regard to interstellar OH masers, they only present the excitation rates from the lowest rotational level ($J = 3/2$, $^2\Pi_{3/2}$) to the next rotational level in $^2\Pi_{3/2}$ and the first two rotational levels of the $^2\Pi_{1/2}$ ladder. These rate constants are comparable in magnitude to those for collisions with H_2 for the same transitions. Collisions with H also produce unequal populations in the Λ-doublet levels, although for a given collisional transition the propensity is sometimes different than for collisions with H_2. A more complete set of calculated rate constants is needed to assess the rotational excitation and Λ-doublet asymmetries for collisions with atomic hydrogen.

REFERENCES

Ádámkovics, M., Glassgold, A. E., & Najita, J. R. 2014, ApJ, 786, 135
A'Hearn, M. F., Millis, R. C., Schleicher, D. O., Osip, D. J., & Birch, P. V. 1995, Icar, 118, 223
Alexander, M. H., Andresen, P., Bacis, R., et al. 1988, JChPh, 89, 1749
Alexander, M. H., & Dagdigian, P. J. 1984, JChPh, 80, 4325
Alexander, M. H., Rackham, E. J., & Manolopoulos, D. E. 2004, JChPh, 121, 5221
Andresen, P., Ondrey, G. S., & Titze, B. 1983, PhRvL, 50, 486
Andresen, P., Ondrey, G. S., Titze, B., & Rothe, E. W. 1984, JChPh, 80, 2548
Atahan, S., & Alexander, M. H. 2006, JPCA, 110, 5436
Banzatti, A., Meyer, M. R., Bruderer, S., et al. 2012, ApJ, 745, 90
Bethell, T., & Bergin, E. 2009, Sci, 326, 1675
Biscaya, A. M., Rieke, G. H., Narayanan, G., Luhman, K. L., & Young, E. T. 1997, ApJ, 491, 359
Bonev, B. P., & Mumma, M. J. 2006, ApJ, 653, 788
Bonev, B. P., Mumma, M. J., DiSanti, M. A., et al. 2006, ApJ, 653, 774
Brown, J. M., Hougen, J. T., Huber, K.-P., et al. 1975, JMoSp, 55, 500
Butler, J. E., Jursich, G. M., Watson, I. A., & Wiesenfeld, J. R. 1986, JChPh, 84, 5365
Carr, J. S. 1989, ApJ, 345, 522
Carr, J. S., & Najita, J. R. 2008, Sci, 319, 1504
Carr, J. S., & Najita, J. R. 2011, ApJ, 733, 102
Carr, J. S., Tokunaga, A. T., & Najita, J. R. 2004, ApJ, 603, 213
Cheng, Y., Yuan, K., Cheng, L., et al. 2011, JChPh, 134, 064301
Cleveland, C. B., Jursich, G. M., Trolier, M., & Wiesenfeld, J. R. 1987, JChPh, 86, 3253
Combi, M. R., Harris, W. M., & Smyth, W. H. 2004, in Comets II, ed. M. C. Festou, H. U. Keller, & H. A. Weaver (Tucson, AZ: Univ. Arizona Press), 523
Crovisier, J. 1989, A&A, 213, 459
Crovisier, J., Colom, P., Gérard, E, Bockelée-Morvan, D., & Bourgois, G. 2002, A&A, 393, 1053
Dixon, R. N. 1985, MoPh, 54, 333
Dixon, R. N. 1995, JChPh, 102, 301
Dixon, R. N. 1999, Sci, 285, 1249
Doppmann, G. W., Najita, J. R., Carr, J. S., & Graham, J. R. 2011, ApJ, 738, 112
Fedele, D., Bruderer, S., van Dishoeck, E. F., et al. 2013, A&A, 559, 77
Feldman, P. D., Cochran, A. L., & Combi, M. R. 2004, in Comets II, ed. M. C. Festou, H. U. Keller, & H. A. Weaver (Tucson, AZ: Univ. Arizona Press), 425
Fillion, J. H., van Harrevelt, R., Ruiz, J., et al. 2001, J. Phys. Chem., 105, 11414
France, K., Schindhelm, E., Burgh, E. B., et al. 2011a, ApJ, 734, 31
France, K., Schindhelm, E., Herczeg, G. J., et al. 2012, ApJ, 756, 171
France, K., Yang, H., & Linsky, J. L. 2011b, ApJ, 729, 7
Gorti, U., Hollenbach, D., Najita, J., & Pascucci, I. 2011, ApJ, 735, 90
Grunewald, A. U., Gericke, K.-H., & Comes, F. J. 1987, CPL, 133, 501
Guedel, M., Lahuis, F., Briggs, K. R., et al. 2010, A&A, 519, 113
Harich, S. A., Hwang, D. W. H., Yang, X., et al. 2000, JChPh, 113, 10073
Hartigan, P., Edwards, S., & Ghandour, L. 1995, ApJ, 452, 736
Häusler, D., Andresen, P., & Schinke, R. 1987, JChPh, 87, 3949
Horne, D., Gibb, E., Rettig, T. W., et al. 2012, ApJ, 754, 64
Houck, J. R., Roellig, T. L., van Cleve, J., et al. 2004, ApJS, 154, 18
Hwang, D. W., Yang, X. F., Harich, S., Lin, J. J., & Yang, X. 1999, JChPh, 110, 4123
Knez, C., Carr, J., Najita, J., et al. 2007, BAAS, 211, 5005
Liu, X., Lin, J. J., Harich, S., Schatz, G. C., & Yang, X. 2000, Sci, 289, 1536
Mikulecky, K., & Gericke, K. 1992, JChPh, 96, 7490
Mordaunt, D. H., Ashford, M. N. R., & Dixon, R. N. 1994, JChPh, 100, 7360
Najita, J. R., Ádámkovics, M., & Glassgold, A. E. 2011, ApJ, 743, 147
Najita, J. R., Carr, J. S., Strom, S. E., et al. 2010, ApJ, 712, 274
Najita, J. R., Edwards, S., Basri, G., & Carr, J. 2000, in Protostars and Planets IV, ed. V. Mannings, A. Boss, & S. Russell (Tucson, AZ: Univ. Arizona Press), 457
Offer, A. R., & van Dishoeck, E. F. 1992, MNRAS, 257, 377
Offer, A. R., van Hemert, M. C., & van Dishoeck, E. F. 1994, JChPh, 100, 362
Podio, L., Kamp, I., Codella, C., et al. 2013, ApJL, 766, L5
Podio, L., Kamp, I., Flower, D., et al. 2012, A&A, 545, A44
Pontoppidan, K. M., Salyk, C., Blake, G. A., & Kaufl, H. K. 2010a, ApJL, 722, L173
Pontoppidan, K. M., Salyk, C., Blake, G. A., et al. 2010b, ApJ, 720, 887
Rothman, L. S., Gordon, I. E., Barber, R. J., et al. 2010, JQSRT, 111, 2139
Rothman, L. S., Jacquemart, D., Barbe, A., et al. 2005, JQSRT, 96, 139
Salyk, C., Pontoppidan, K. M., Blake, G. A., et al. 2008, ApJL, 676, L49
Salyk, C., Pontoppidan, K. M., Blake, G. A., Najita, J. R., & Carr, J. C. 2011, ApJ, 731, 130
Schindhelm, E., France, K., Burgh, E. B., et al. 2012a, ApJ, 746, 97
Schindhelm, E., France, K., Herczeg, G. J., et al. 2012b, ApJ, 756, 23
Smith, G. K., & Butler, J. E. 1980, JChPh, 73, 2243
Tappe, A., Forbrich, J., Martín, S., Yuan, Y., & Lada, C. J. 2012, ApJ, 751, 9
Tappe, A., Lada, C. J., Black, J. H., & Muench, A. A. 2008, ApJL, 680, L117
van der Loo, M., & Groenenboom, G. 2007, JChPh, 126, 114314
van der Tak, F. F. S., Black, J. H., Schöier, F. L., Jansen, D. J., & van Dishoeck, E. F. 2007, A&A, 468, 627
Wu, C. Y., & Chen, F. Z. 1993, JGRE, 98, 7415
Yang, H., Herczeg, G. J., Linsky, J., et al. 2012, ApJ, 2012, 121
Yang, X. F., Hwang, D. W., Lin, J. J., & Ying, X. 2000, JChPh, 113, 10597
Yuan, K., Cheng, L., Cheng, Y., et al. 2009, JChPh, 131, 74301
Zanganeh, A. H., Fillion, J. H., Ruiz, J., et al. 2000, JChPh, 112, 5660